The Astrophysical Journal, 838:134 (16pp), 2017 April 1 https://doi.org/10.3847/1538-4357/aa6682

Triggering Process of the X1.0 Three-ribbon Flare in the Great Active Region NOAA 12192

Yumi Bamba[1,2], Satoshi Inoue[2], Kanya Kusano[2], and Daikou Shiota[2]
[1] Institute of Space and Astronautical Science (ISAS)/Japan Aerospace Exploration Agency (JAXA) 3-1-1 Yoshinodai, Chuo-ku, Sagamihara, Kanagawa 252-5210, Japan; y-bamba@nagoya-u.jp
[2] Institute for Space-Earth Environmental Research (ISEE)/Nagoya University Furo-cho, Chikusa-ku, Nagoya, Aichi 464-8601, Japan
Received 2015 July 23; revised 2017 February 7; accepted 2017 March 11; published 2017 April 3

Abstract

The solar magnetic field in a flare-producing active region (AR) is much more complicated than theoretical models, which assume a very simple magnetic field structure. The X1.0 flare, which occurred in AR 12192 on 2014 October 25, showed a complicated three-ribbon structure. To clarify the trigger process of the flare and to evaluate the applicability of a simple theoretical model, we analyzed the data from *Hinode*/Solar Optical Telescope and the *Solar Dynamics Observatory*/Helioseismic and Magnetic Imager, Atmospheric Imaging Assembly. We investigated the spatio-temporal correlation between the magnetic field structures, especially the non-potentiality of the horizontal field, and the bright structures in the solar atmosphere. As a result, we determined that the western side of the positive polarity, which is intruding on a negative polarity region, is the location where the flare was triggered. This is due to the fact that the sign of the magnetic shear in that region was opposite that of the major shear of the AR, and the significant brightenings were observed over the polarity inversion line (PIL) in that region before flare onset. These features are consistent with the recently proposed flare-trigger model that suggests that small reversed shear (RS) magnetic disturbances can trigger solar flares. Moreover, we found that the RS field was located slightly off the flaring PIL, contrary to the theoretical prediction. We discuss the possibility of an extension of the RS model based on an extra numerical simulation. Our result suggests that the RS field has a certain flexibility for displacement from a highly sheared PIL, and that the RS field triggers more flares than we expected.

Key words: Sun: activity – Sun: flares – Sun: magnetic fields – sunspots

Supporting material: animation

1. Introduction

The triggering mechanisms of solar flares are not yet completely understood. Many previous studies have attempted to reveal the physics of solar flare occurrence using theoretical and/or observational methods (e.g., Antiochos et al. 1999; Chen & Shibata 2000; Moore et al. 2001). Currently, the CSHKP model (Carmichael 1964; Sturrock 1966; Hirayama 1974; Kopp & Pneuman 1976) is widely accepted to be the standard solar flare model. In this model, magnetic reconnection plays an important role in the energy release process of the solar flare, and it is substantiated by the *Yohkoh* satellite (Ogawara et al. 1992) observations. *Yohkoh* captured a bright cusp structure in the solar corona with soft X-ray observations (Tsuneta et al. 1992), and it is believed to be evidence of energy release by magnetic reconnection (Tsuneta 1996). However, we still do not know what triggers the magnetic reconnection process, although there are several candidates, such as emerging flux (e.g., Heyvaerts et al. 1977; Kurokawa et al. 2002), flux cancellation (e.g., Zhang 2001; Green et al. 2011), sunspot rotation (e.g., Louis et al. 2014), shear motion (e.g., Hagyard et al. 1984; Kusano et al. 1995), and the reversal of shear (Kusano et al. 2004). The quantitative conditions of each flare-trigger model have not yet been clarified. This might be the cause of our limited capacity for flare forecasting.

Kusano et al. (2012) performed a new numerical simulation to investigate the triggering of solar flares. They used a simple magnetic field structure and characterized it using two parameters: the global magnetic shear angle θ of the active region (AR) and the azimuth ϕ of the small bipole appearing on the polarity inversion line (PIL; see Figure 1 in Kusano et al. 2012 and Bamba et al. 2013). They surveyed which combination of θ and ϕ can trigger flares, and found that two types of structures, the opposite polarity and the reversed shear (RS), are capable of triggering flares. Bamba et al. (2013) performed an observational verification of the flare-trigger model proposed by Kusano et al. (2012). They analyzed four major flares observed by the *Hinode* satellite (Kosugi et al. 2007) and quantitatively confirmed how the observed results of θ and ϕ are consistent with Kusano et al.'s numerical simulation results. They identified small magnetic bipoles triggering flares in ARs with relatively a simple magnetic field and PIL structure. However, solar flares generally occur in complicated ARs that are very different from the simple structure assumed in the simulation. Therefore, it is important to examine whether the theoretical model is applicable to more complex ARs.

AR NOAA 12192 was the biggest sunspot region in the solar cycle 24. The AR stayed on the solar disk through three Carrington rotations, and it was numbered NOAA 12172 (and 12173), 12192, and 12209 in each phase. AR 12192 had the most complicated magnetic structure including a δ-type sunspot in which several umbrae are sharing a penumbra. A major bipole extended from east to west, and emerging flux was seen in the middle of the bipole. Six X-class flares occurred in the AR during disk passage, and these showed clear flare ribbons appearing in the central region of the AR. In particular, the X1.0 flare on 2014 October 25, which is the fourth X-class flare in the AR, produced three flare ribbons.

Kusano et al. (2012) and Bamba et al. (2013) have demonstrated that the small magnetic bipoles that trigger flares are located in the center of the initial flare ribbons. However, it

Table 1
List of X-class Flares that Occurred in NOAA AR 12192

Date	Start Time[a] (UT)	Peak Time[a] (UT)	End Time[a] (UT)	*GOES* X-ray Class	Location[b]
2014 Oct 19	04:17	05:03	05:48	X1.1	S14E64
2014 Oct 22	14:02	14:28	14:50	X1.6	S14E13
2014 Oct 24	21:07	21:40	22:13	X3.1	S22W21
2014 Oct 25	16:31[c]	17:03[c]	17:07[c]	X1.0	S10W22
2014 Oct 26	10:04	10:56	11:18	X2.0	S14W37
2014 Oct 27	14:02	14:47	15:09	X2.0	S16W56

Notes.
[a] The start, peak, and end times are defined from the X-ray observations of the *GOES* satellite.
[b] http://www.solarmonitor.org/
[c] These times are defined from *RHESSI* observations.

is difficult to infer where in the AR the triggering structure is and to reveal the physical processes for the three-ribbon flare. In this paper, we aim to clarify the X1.0 flare-triggering process in AR 12192 to examine whether the trigger model is applicable even for complicated ARs. Moreover, it should be noted that neither the X1.0 flare nor the other X-class flares in the AR produced any coronal mass ejections (CMEs), although it is reported that statistically, 75% of X-class flares are associated with CMEs (Yashiro et al. 2006). We also discuss why the X1.0 flare did not have associated CMEs from the point of view of the triggering mechanism.

This paper is organized as follows. The sampled data and analysis method are described in Sections 2 and 3, respectively. The data analysis results are shown in Section 4. The conceivable scenarios for the X-class flare and the reason why the flares in the AR are not associated with any CMEs are discussed in Section 5. Finally, we summarize the results and considerations in Section 6.

2. Data Descriptions

More than 130 flares, which were larger than C1.0, occurred in the great AR 12192. Table 1 lists the X-class flares that occurred in this AR. The *Solar Dynamics Observatory* (*SDO*; Pesnell et al. 2012) observed all of the flares, whereas *Hinode*/SOT (Tsuneta et al. 2008) observed the last five. In this paper, we focus on the X1.0 flare on 2014 October 25, which was observed by both *Hinode* and *SDO*. The AR was located at the S10°–20° latitude and W15°–25° longitude during the flare. Figure 1 shows the soft X-ray light curve observed by *Geostationary Operational Environmental Satellite* (*GOES*) 1–8 Å and 0.5–4 Å. The onset time of the X1.0 flare was 16:31 UT[3], and it is indicated by a blue vertical line in Figure 1. The two C-class flares (C5.1 at 15:00 UT and C9.7 at 15:44 UT occurred before the X1.0 flare onset, and these are indicated by the green and red vertical lines.

We analyzed *SDO* data from 13:00 UT to 19:00 UT on October 25. *SDO* observed the full disk of the Sun (2000″ × 2000″), and we used filter magnetograms taken by the Helioseismic and Magnetic Imager (HMI; Schou et al. 2012) at 6173 Å (Fe I line, samples the photospheric magnetic field), and filtergrams taken by the Atmospheric Imaging Assembly (AIA; Lemen et al. 2012) at 1600 Å (continuum and C IV line, samples the upper photosphere and the transition region), 171 Å (Fe IX line, samples the upper transition region

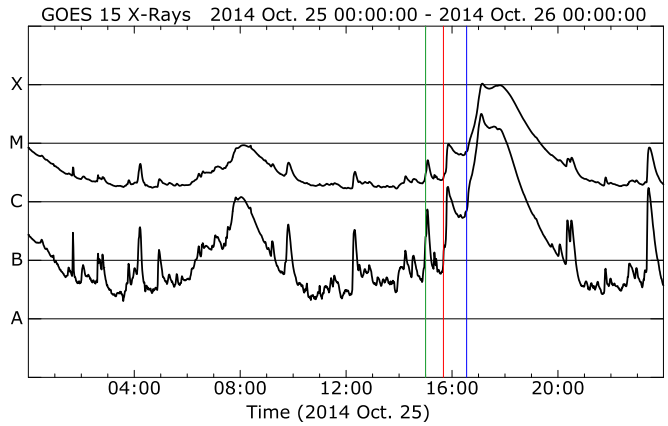

Figure 1. Soft X-ray light curve observed by *GOES* (1–8 Å and 0.5–4 Å) from 00:00 UT on 25 October to 00:00 UT 26 October 2014. The green/red/blue vertical line indicates the onset time of the C5.1 (15:00 UT)/C9.7 (15:44 UT)/X1.0 (16:31 UT) flare, respectively.

and quiet corona), 131 Å (Fe VIII and Fe XXI lines, samples the transition region and flaring corona), 193 Å (Fe XII and Fe XXIV lines, samples the corona and hot flare plasma), and 304 Å (He II line, samples the chromosphere and the transition region). The spatial resolution and the cadence were 1″ and 45 s for HMI, and 1.″5 and 12 s for AIA (except for AIA 1600 Å where the cadence was 24 s). We investigated the spatial and temporal correlation between the evolution of the photospheric magnetic field and brightenings in the chromosphere, the transition region, and the corona.

Moreover, we used vector magnetic field data (the Space-weather HMI AR Patch:SHARP) obtained by *SDO*/HMI on October 25 15:00 UT to calculate the NLFFF. We also used *Hinode*/SOT data to perform more precise analysis of the magnetic field. We used the full polarization states (Stokes-*I, Q, U*, and *V*) at 6301.5 and 6302.5 Å (Fe I line) with a sampling of 21.5 mÅ, obtained by the Spectro-Polarimeter (SP). The SP scanned the central part of the AR at 11:00–11:33 UT with a 164″ × 164″ field of view (FOV), and the spatial resolution was 0.″3.

3. Analysis Methods

3.1. Method of SDO HMI/AIA Analysis

In this study, we basically used the analysis method developed in Bamba et al. (2013). The analysis method was originally developed for *Hinode*/SOT data, but Bamba et al. (2014)

[3] This time is defined from the X-ray observations of the *RHESSI* satellite (*Reuven Ramaty High Energy Solar Spectroscopic Imager*; Lin et al. 2002) because *GOES* likely released wrong times for this event.

already examined the applicability of the analysis method to the *SDO* data sets. Here, we briefly summarize the procedures of the analysis method.

We used HMI level 1.5 line-of-sight (LOS) magnetograms (`hmi.M_45s` series) and AIA level 1.0 data (`aia.lev1_euv_12s` and `aia.lev1_uv_24s` series). We first calibrated all the HMI filter magnetograms and all the AIA images using the `aia_prep` procedure in the Solar Soft-Ware (SSW) package. By this process, spatial fluctuations were reduced, and the images were rotated so that the solar EW and NS axes are aligned with the horizontal and vertical axes of the image, respectively. Moreover, LOS magnetograms and AIA images were resampled to the same size because the pixel scales are different between HMI and AIA. Thus, the positions of the LOS magnetograms and AIA images were aligned. Next, we chose an HMI filter magnetogram and an AIA image closest in time, and these two images were superimposed on each other. We drew the PILs and the strong emission contours in the AIA image on the LOS magnetogram at each time. The PILs were drawn on the AIA images at each time as well.

3.2. Method of Hinode/SOT Analysis

The SP scan data were calibrated using the `sp_prep` procedure (Lites & Ichimoto 2013) in the SSW package assuming a Milne–Eddington atmosphere. The inversion code MEKSY (developed by Dr. Takaaki Yokoyama) was adopted, and the 180° ambiguity in the vector magnetograms is resolved using the AZAM utility (Lites et al. 1995). Note that the observed "LOS" and "transverse" magnetic field vectors (i.e., image-plane magnetic field) were converted to the heliographic magnetic field B_x, B_y, and B_z using Equation (1) of Gary & Hagyard (1990).

We investigated the distribution of the magnetic shear over the AR before the flare onset, using the vector magnetogram obtained from the SP scan data. We first calculated the potential field using the `fff` procedure in the `nlfff` package (developed by Dr. Yuhong Fan) in SSW. Then we measured the angles between the potential field vector $\boldsymbol{B}_p$ and horizontal field vector $\boldsymbol{B}_h = \sqrt{B_x{}^2 + B_y{}^2}$ in each pixel, and we defined these angles as the relative shear angle χ. The relative shear angles are defined between $\pm 180°$, where 0° means vectors $\boldsymbol{B}_p$ and $\boldsymbol{B}_h$ are oriented in the same direction. The direction of the vector $\boldsymbol{B}_h$ deviates from that of the vector $\boldsymbol{B}_p$ counterclockwise (clockwise) when the magnetic helicity is positive (negative) and the value of χ is positive (negative). We colorize the relative shear angles, as shown in Section 4.3.

4. Results

4.1. Overview of the C5.1, C9.7, and X1.0 Flares in Each Wavelength

The temporal evolution of the brightenings and flare ribbons in AIA 1600 Å, which is sensitive to the emission from the upper chromosphere and the transition region, is shown in Figure 2. We can see the contours of those brightenings with the magnetic field structure in Figure 3, where white/black indicates the positive/negative polarity of the LOS magnetic field. The green lines and the red contours denote the PIL (line of 0 G) and the significant brightenings (2000 DN) in AIA 1600 Å, respectively. The green lines in Figure 2 are the same as those in Figure 3. The positive polarity that is intruding on the negative region N1 (henceforth IPP: intruding positive polarity) and the weak negative region N2 is located between the major bipole P1 and N1, as can be seen in Figure 3(a). We can also see the small brightenings B1 and B2, which are indicated by the yellow arrows in panel (a) of both Figures 2 and 3. These brightenings are seen intermittently at the west side of the IPP at 14:48–14:58 UT. The other brightening B3 is also seen in the IPP in panel (a). The flare ribbons of the C5.1 flare appear about five minutes later, as shown in panel (b). The positive ribbons CR1 and CR2 are clearly seen in the P1 and IPP regions. There are two negative ribbons in the N1 region, but these brightenings are connected to each other in the AIA 304 Å image (see Figure 4(b) and the following description). We then identify these brightenings in the N1 region as the negative ribbon CR3, as seen in Figure 2(b). B1 and B2 disappear in the last minute before the C5.1 flare, while B3 enhances as the flare ribbon CR2 in panel (b). It is inferred that B1 and B2 are caused by a local magnetic reconnection that occurred at the west side of the IPP before the C5.1 flare onset, and that the B1 and B2 brightenings appear at the footpoints of the small magnetic loops connecting the IPP and N2. It is also suggested that B3 is located at the footpoint of the magnetic loop that connects the IPP and N1 and which corresponds to the C5.1 flare. Once the three ribbons CR1, CR2, and CR3 of the C5.1 flare disappear by 15:15 UT, the C9.7 flare ribbons appear from 15:40 UT as seen in panel (c). The C9.7 flare also shows three flare ribbons CR1, CR2, and CR3 at the same location as the ribbons of the previous C5.1 flare. The three ribbons of the C5.1 and C9.7 flares almost never propagate with time. A faint ribbon-like brightening remained at the region where CR1 is seen even after the three ribbons disappeared, as seen in Figure 2(d). Panel (e) shows the initial flare ribbons of the X1.0 flare that appear about one hour after the C9.7 flare. In this phase, XR1 (positive ribbon) and XR2 (negative ribbon) at the west side/middle are more clearly seen than XR3 (negative ribbon) at the east side. These three ribbons slowly grow between 16:35–17:10 UT as shown in panel (f). In particular, XR1 and XR3 get longer in the southward and northward directions, respectively. However, they almost never propagate to the outer sides (i.e., westward and eastward) with time. XR2 disappears first in the late phase, while XR1 and XR3 remain more than one hour after the flare onset.

Figure 4 shows the AIA 304 Å images with the same FOV and almost the same time as Figures 2 and 3. The PILs are overplotted only in panel (a). The intermittent brightenings B1, B2, and B3 are indicated by the yellow arrows in panel (a), and these are seen at the west side of the IPP as well as shown in the AIA 1600 Å image of Figure 2(a). The brightenings B1 and B2 are connected to each other via a small loop striding over the local PIL at the west side of the IPP. It is clearly seen at 14:48–15:00 UT although it persisted from 13:00 UT to just before the onset of the C5.1 flare. It also suggests the existence of small magnetic loops that connect the IPP and N2 on the west side of the IPP. On the other hand, the brightening B3 is connected with N1, where CR3 will appear, as clearly seen in Figures 4(a) and (b). The brightenings, which will be the flare ribbons CR1 and CR2, are already seen from 13:00 UT, and CR3 also appears from 14:00 UT. The three ribbons start becoming enhanced from 14:30 UT, and these will be the three ribbons of the C5.1 flare in panel (b). There is a filament on the PIL between P1 and N2, and some bright points start to move

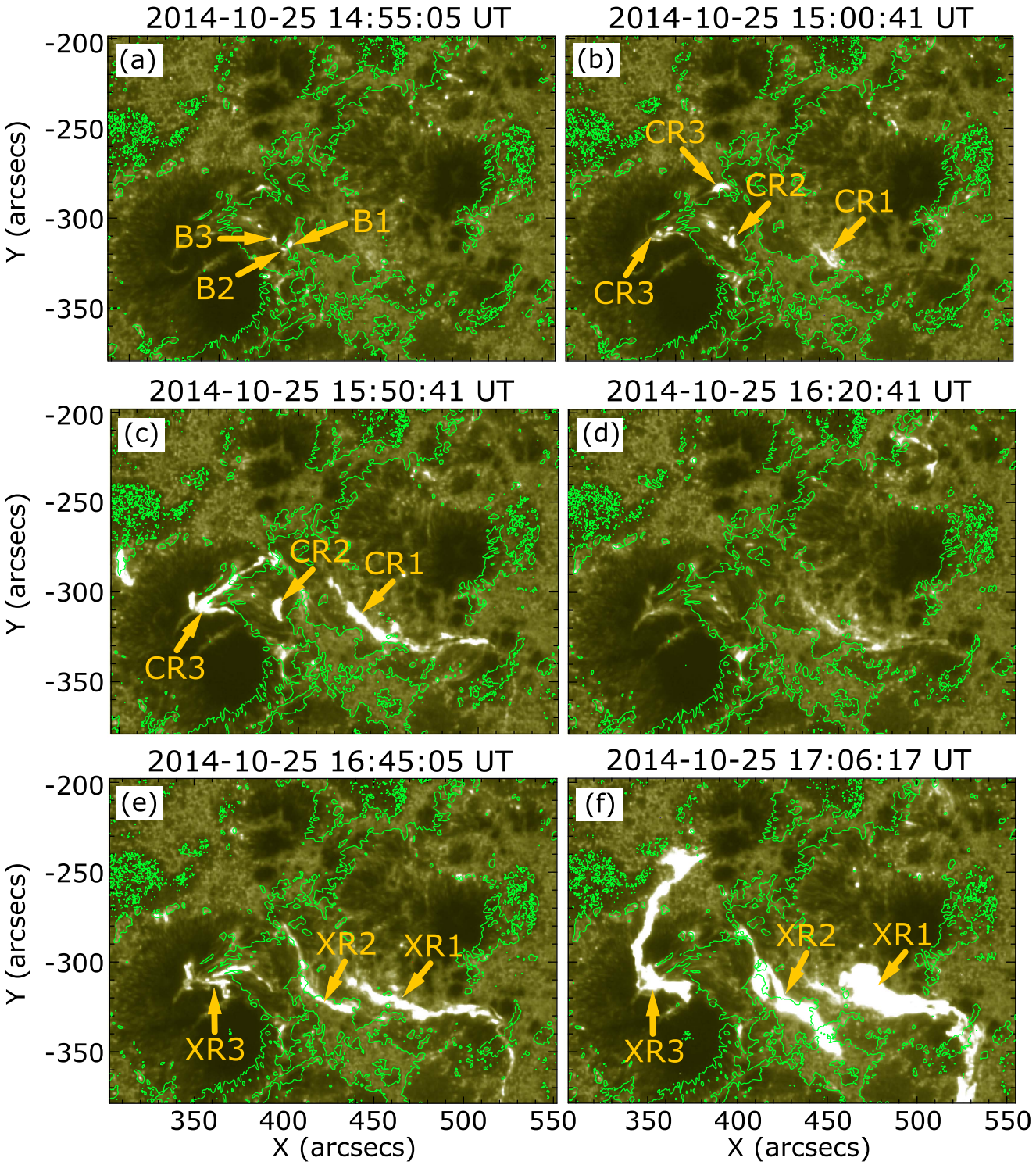

Figure 2. Temporal evolution of the significant brightenings in the upper photosphere and transition region, and the flare ribbons in AIA 1600 Å images. Green lines indicate the PILs in the HMI LOS magnetograms at each time. The intensity scale range is 0–2000 DN. (a) Strong brightenings are intermittently seen at the west side of the IPP as indicated by the yellow arrow. (b) The three ribbons (CR1–CR3) of the C5.1 flare. (c) The three ribbons (CR1–CR3) of the C9.7 flare. (d) A faint ribbon-like brightening remains at the region where CR1 is seen. (e) The initial three ribbons of the X1.0 flare. XR1 is the positive ribbon, and XR2 and XR3 are the negative ribbons. (f) Enhanced three-ribbon emission of the X1.0 flare.

along the filament just before the C5.1 flare (from 14:58 UT). The three ribbons CR1, CR2, and CR3 remain even after the onset of the C5.1 flare, and the bright point motion along the filament continues and becomes intense. These bright structures flow down along the filament to the footpoints in the P1 and N1 regions, and then the three ribbons CR1, CR2, and CR3 of the C9.7 flare are enhanced from 15:47 UT (see panel (c)). Note that the strong brightening, which looks like another flare ribbon between CR1 and CR2 in panel (c), is not a flare ribbon, but a bright point moving along the filament like the tether-cutting reconnection (see Figure 6 and the following description). The flare ribbons remain clearer than those seen in Figure 2(c),

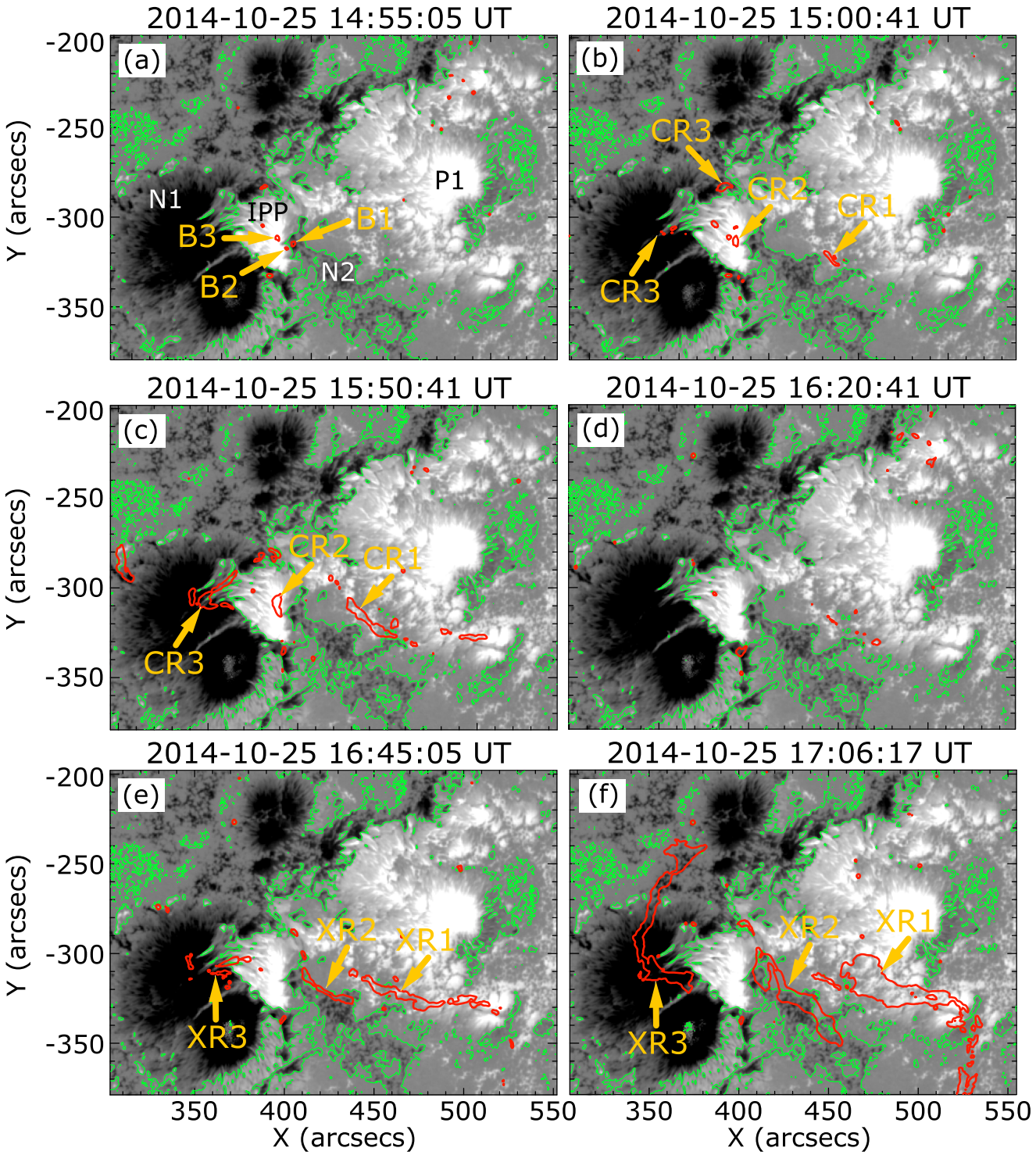

Figure 3. Temporal evolution of the HMI LOS magnetic field at ±1000 G. White/black indicates the positive/negative polarity of the LOS magnetic field, and the green lines indicate the PILs. The red contours outline the brightenings in AIA 1600 Å images with an intensity of 2000 DN. The time of each panel is the same as that of the AIA 1600 Å images. Panels (a)–(f) show the same features as Figure 2 together with the LOS magnetic field.

especially CR1 and CR3, which are clearly seen in Figure 4(d). The remaining ribbons are enhanced and a new flare ribbon along the filament gradually appeared in the N2 region from 16:30 UT, becoming XR2 in panel (e). This is the X1.0 flare, and the flare ribbons XR1 and XR3 correspond to CR1 and CR3, respectively. CR2 also remains, but it is not seen in the AIA 1600 Å images (see Figures 2(e) and (f)). In the initial phase of the X1.0 flare (until 16:55 UT), the ex-CR2 brightening and the negative ribbon XR3 are connected, as seen in Figure 4(e). It corresponds to the first peak of the X1.0 flare in the *GOES* soft X-ray light curve (cf. Figure 1). Then, the bright bridge connecting ex-CR2 and XR3 weakened, and XR3 becomes longer to the north as seen in panel (f). XR1 and XR2 are also enhanced at that time, and the post-flare loop connecting

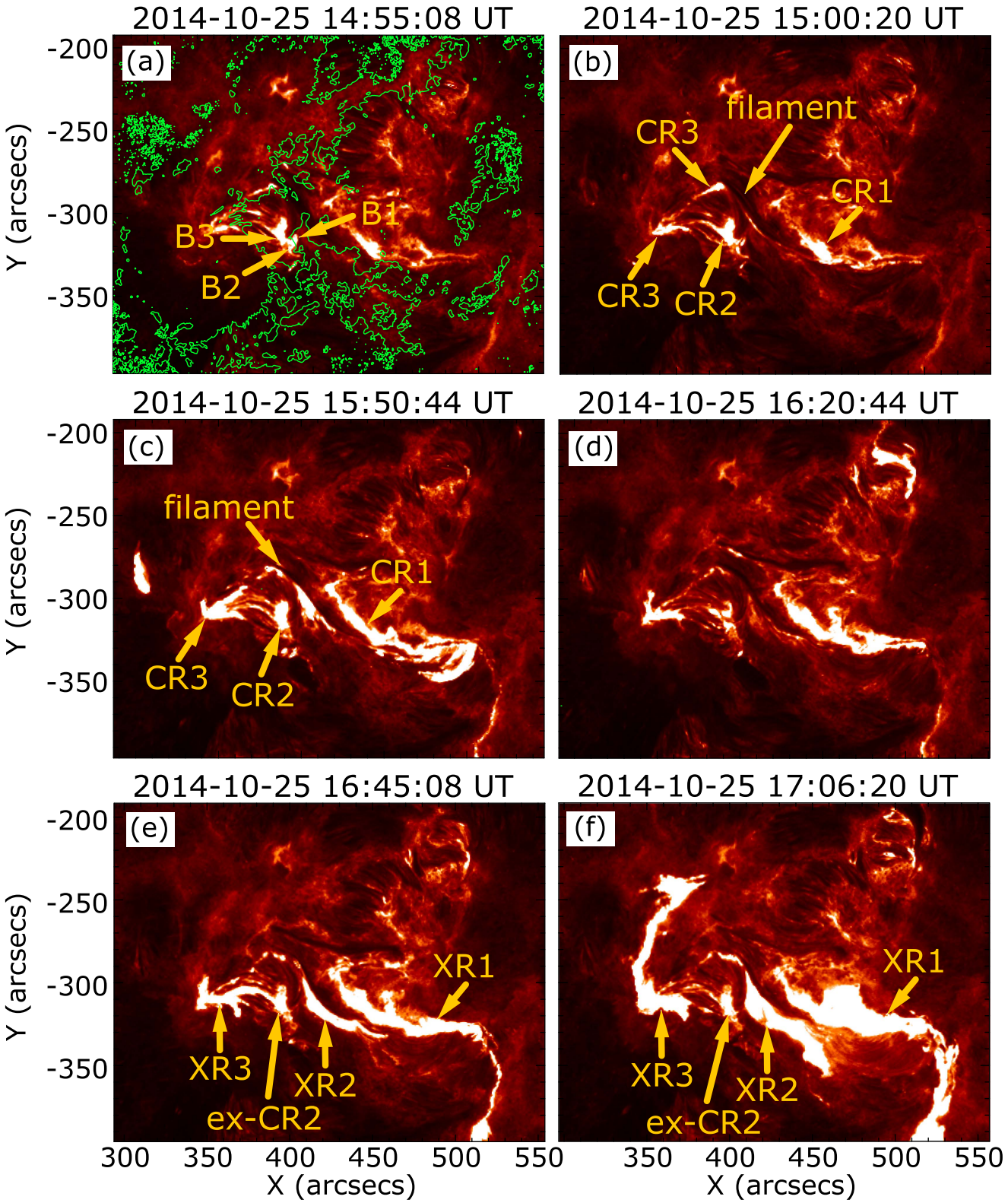

Figure 4. Temporal evolution of the chromospheric brightenings and flare ribbons in AIA 304 Å images. The PILs are overplotted with green lines in panel (a). The intensity scale range is 0–1000 DN. Panels (a)–(f) show almost the same features as Figure 2, but the brightening B1 and B2 are connected to each other via a small loop striding over the local PIL at the west side of the IPP. Moreover, the CR1 ribbon here remains clearer than that seen in Figure 2(c), and CR3 also remains in panel (d).

XR1 and XR2 appeared. XR2 is weakened first while XR1 and XR3 likewise remain in the AIA 1600 Å images.

The coronal loops in the AIA 131 Å images are shown in Figure 5, with the PILs only shown in panel (a). In the early phase (panel (a)), the bright loops L1 and L2 connect IPP–N1 and P1–N1, respectively. The IPP has continuously emerged from October 19, and it has intruded onto the negative sunspot (N1). Therefore, it is suggested that a strong electric current

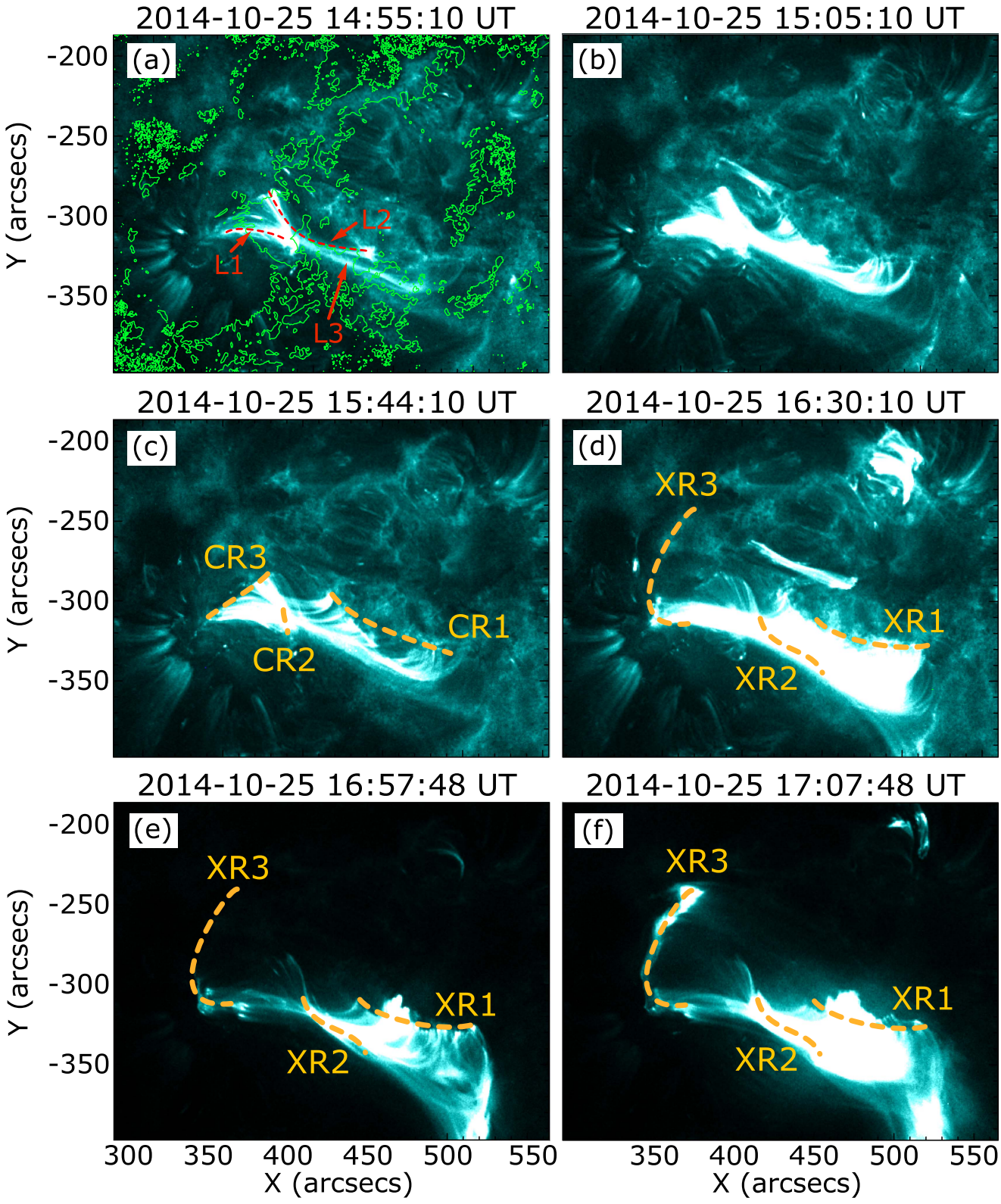

Figure 5. Temporal evolution of the coronal loops in AIA 131 Å images. The PILs are overplotted with green lines in panel (a). The intensity scale range is 0–500 DN. The bright loops L1 and L2, which connect IPP–N1 and P1–N1, are outlined by red broken lines in panel (a). The other loop L3 likely connects P1–N2. The yellow broken lines roughly illustrate the locations of the three ribbons of C9.7 in panel (c) and the locations of the three ribbons of X1.0 in panels (d)–(f).

layer is formed in between L1/L2 and the overlying magnetic arcade that connects P1–N1 (it is located higher/more outside than L2). In this layer, coronal loops are heated by the magnetic reconnection between L1/L2 and the overlying magnetic arcade, even though the field directions of the magnetic loops do not differ strongly. Note that there is another faint loop, L3, indicated in panel(a), and it might connect P1–N2 (and also P1–N1). The footpoints of L1 and L2 brighten as seen in

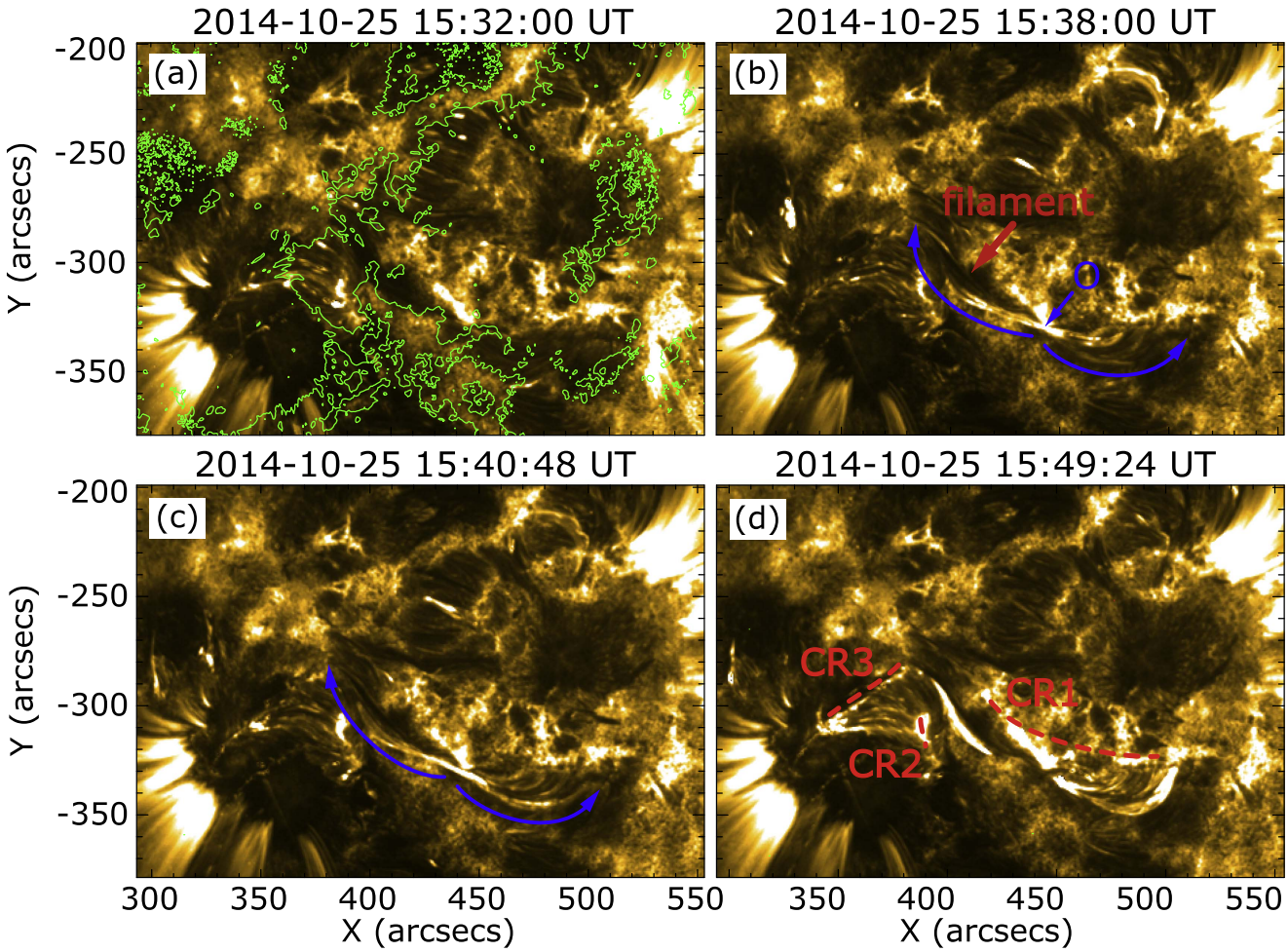

Figure 6. Tether-cutting magnetic reconnection in the AIA 171 Å images. The FOV is almost the same as in Figures 2–5. The intensity scale range is 0–5000 DN, and the PILs are overplotted as the green lines in panel (a). (b) Faint loop structures intersect at point O (indicated by the blue arrow), and small brightenings frequently move along the faint loops. (c) The motion along the loop, such as that illustrated by the blue arrows, is enhanced, and the loops slightly expand. (d) CR1 and CR3 appear at the footpoints of the faint loops as indicated by the red broken lines (Movie 1).

(An animation of this figure is available.)

Figure 4(a). These heated loops L1 and L2 are enhanced at the onset of the C5.1 flare as seen in Figure 5(b). Once the intensity of the coronal loops decrease at 15:15–15:35 UT, the loops L1 and L2 become bright again, and the three ribbons of the C9.7 flare appear as indicated by the yellow broken lines in panel (c). Then, the intensity of the coronal loops continuously increases until the onset time of the X1.0 flare (panel (d)). The coronal loops connecting XR1 and XR2 enhance (panel (e)), XR3 appears, and the faint coronal loops connecting XR1 and XR3 can be seen in panel (f).

Interestingly, the tether-cutting magnetic reconnection process (Moore et al. 2001) is clearly seen between the C5.1 and C9.7 flares. Figure 6 shows the AIA 171 Å images with a similar FOV to Figures 2–5. The PILs are overplotted only in panel (a), and there is a filament as indicated by the red arrow in panel (b). We can see the faint loop structures that intersect at point O and along the filament. Some small brightenings frequently move along these faint loops as illustrated by the blue arrows in panel (b). These bright structures are seen from 13:00 UT, and these are enhanced from 15:00 UT, just before the C5.1 flare. The motion along the loops becomes faster, and the loops slightly expand between 15:40 and 16:00 UT (panel (c)). The flare ribbons CR1 and CR3 of the C9.7 flare appear at the footpoints of the faint loops, as illustrated by the red broken lines in panel (d), and we can see the three ribbons in the chromosphere at that time (see Figure 4(b)). These are clearly seen in Movie 1. A similar motion of the bright structure along the filament is also seen in the AIA 304 Å images just after the C5.1 flare to the onset of the C9.7 flare. It suggests that the tether-cutting magnetic reconnection occurs in the C5.1 and C9.7 flares at point O.

The bright points B1, B2, and B3; the tether-cutting reconnection; and the bright coronal loops connecting XR1 and XR2 are also seen in the AIA 193 Å images (Figure 7) with much less saturation. In panel (a), the brightenings B1, B2, and B3 are clearly seen, and they are also seen in the AIA 1600 and 304 Å images. The brightening B3 corresponds to the positive footpoint of the coronal loop L1 that connects the IPP and N1 (cf. Figure 5(a)). The positive footpoint of L2 is also seen as a bright point in the P1 region, as seen in Figure 7(a). The tether-cutting reconnection is also seen in panel (b), although it is fainter than that seen in the AIA 304 and 171 Å images. After the tether-cutting reconnection, from 16:30 UT, the faint coronal loops rooted in XR1 and XR2 drastically expand to the southwest, as illustrated by the blue arrow in panel (c). This expanding motion of the faint coronal loops

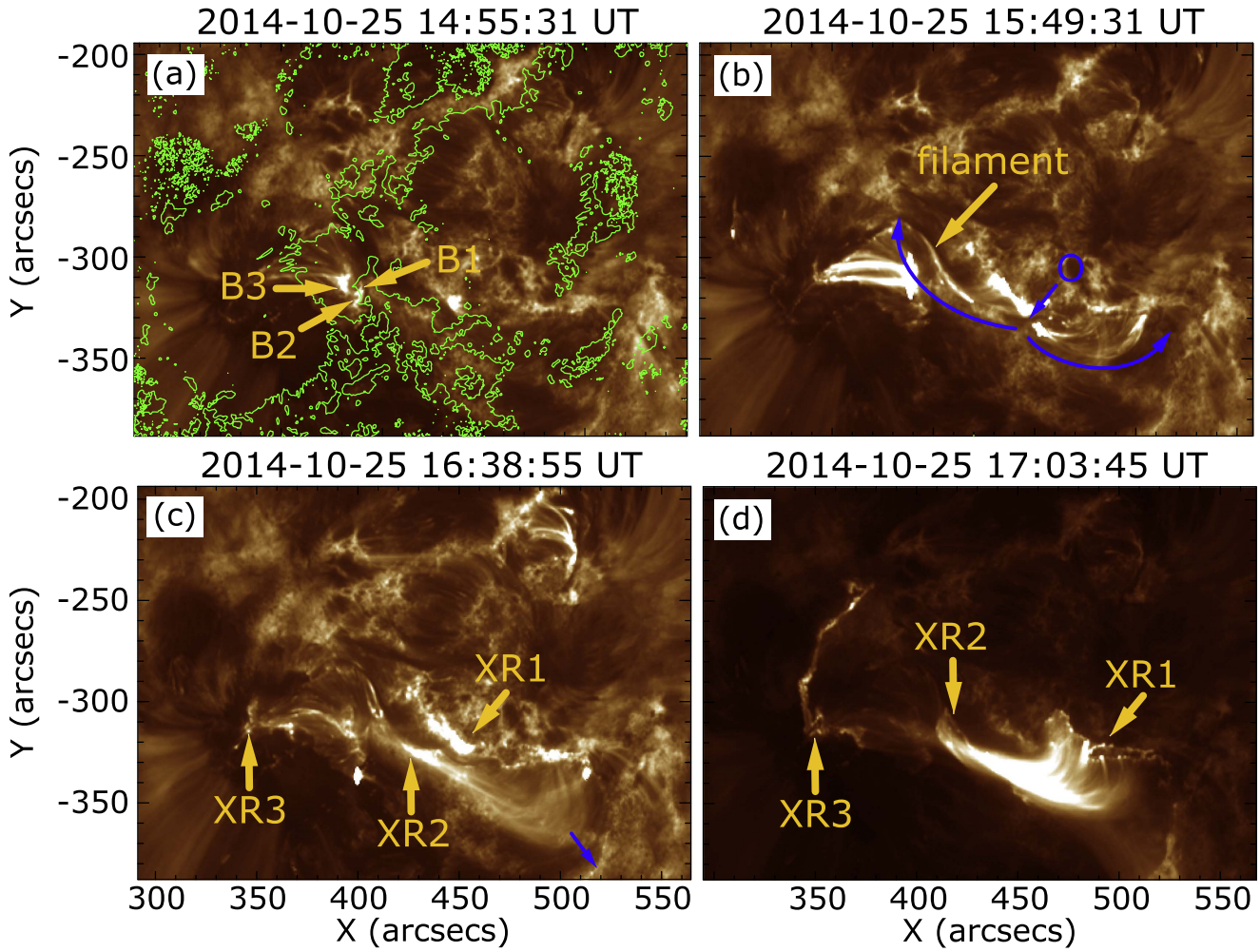

Figure 7. Evolution of the coronal loops and brightenings in the AIA193 Å images. The FOV is almost the same as in Figures 2–5. The intensity scale range is 0–8000 DN, and the PILs are overplotted as the green lines in panel (a).

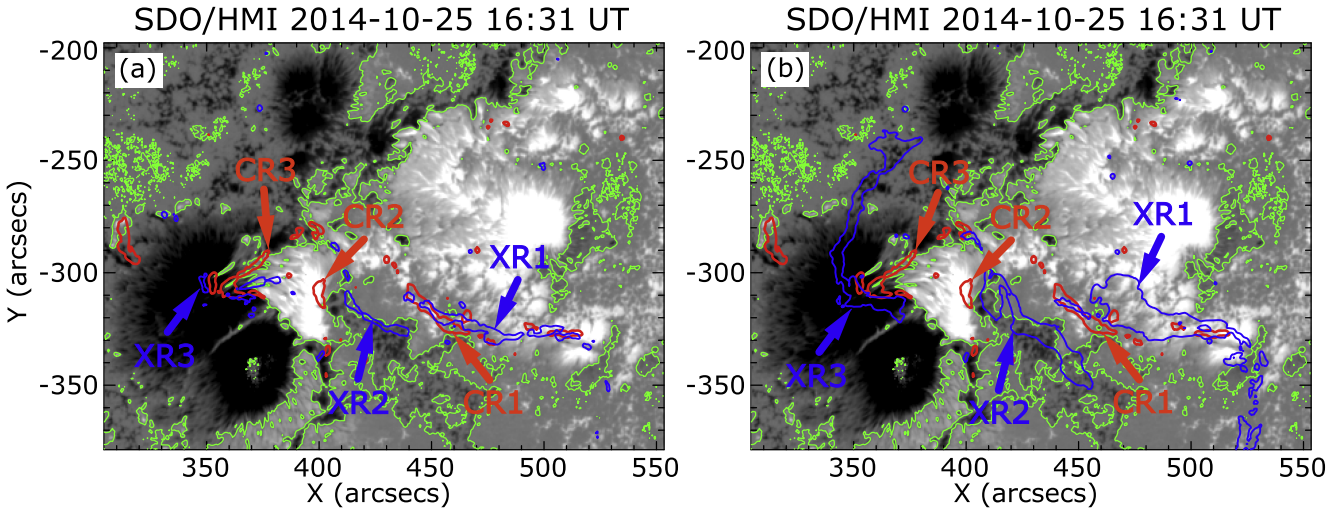

Figure 8. Flare ribbons of the C9.7 and X1.0 flares. The background images are HMI LOS magnetograms at the onset time of the X1.0 flare (16:31 UT on 2014 October 25). The green lines are the PILs, and the red/blue contours outline the flare ribbons in AIA 1600 Å images. The red contour shows CR1, CR2, and CR3 of the C9.7 flare at 15:50 UT in both panels (a) and (b). The blue contour outlines the initial flare ribbons (XR1–XR3) of the X1.0 flare at 16:45 UT in panel (a), while the enhanced flare ribbons at 17:06 UT are outlined in panel (b).

correspond to the enhancement of the coronal loops seen in Figures 5(d)–(f). Then, the flare ribbons XR1 and XR3 elongate southward and northward, respectively.

4.2. Locations of the C9.7 and the X1.0 Flare Ribbons

The flare ribbons of the two C-class flares (the C5.1 and C9.7 flares) appear at the same location, as we described in the

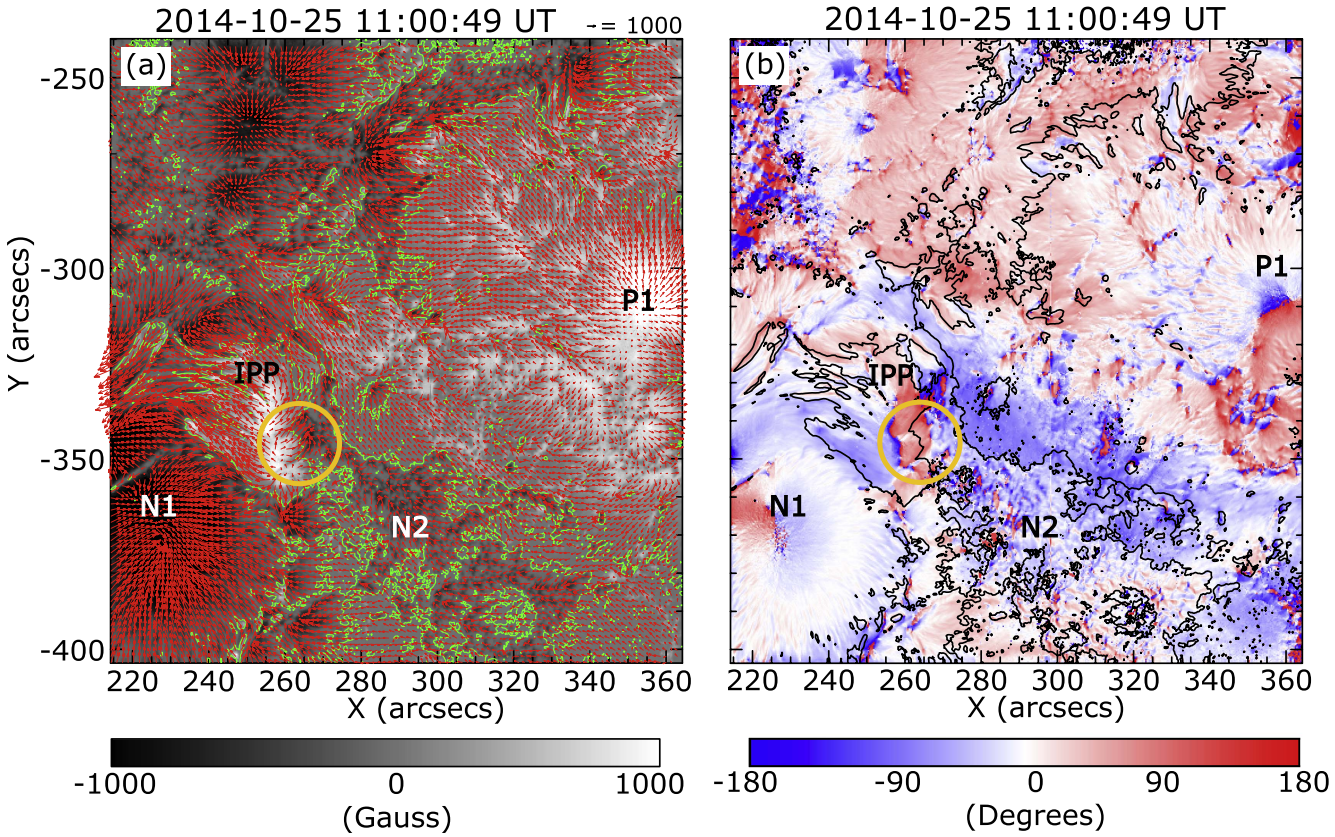

Figure 9. (a) Distribution of the heliographic magnetic field obtained by *Hinode*/SP between 11:00 and 11:33 UT on 2014 October 25. The grayscale corresponds to the positive/negative polarity of B_z at ±2000 G. Green lines indicate the PILs (line of $B_z = 0$ G), and the red arrows are the vectors of the horizontal magnetic field $\boldsymbol{B}_h = \sqrt{{B_x}^2 + {B_y}^2}$ at each point. (b) Distribution of the relative shear angle χ, which is defined as the angle between the potential field vector $\boldsymbol{B}_p$ and horizontal field vector $\boldsymbol{B}_h$. The black lines are the PILs, which are indicated by green lines in panel (a). Red/blue corresponds to positive/negative values of χ, i.e., the magnetic helicity. The region where the strong chromospheric emissions were seen is delineated by the yellow circle in both (a) and (b).

previous section. Therefore, here we compare the locations and evolution between the C9.7 and X1.0 flare ribbons. Figure 8 shows the distribution of the C9.7 and X1.0 flare ribbons. The background images are the HMI LOS magnetograms at the onset time of the X1.0 flare (16:31 UT), and the green lines indicate the PILs. The red contour outlines the brightenings in AIA 1600 Å, such as the flare ribbon at 15:50 UT (just after the C9.7 flare onset), in both panels (a) and (b). The blue contours outline the brightenings at 16:45 UT (before the X1.0 flare onset) in panel (a) and at 17:06 UT (after the X1.0 flare onset) in panel (b), respectively. The initial flare ribbons of the C9.7 and X1.0 flares are seen in panel (a). XR1 and XR3 of the X1.0 flare are located slightly to the outer side of CR1 and CR3 of the C9.7 flare. XR1, XR3, CR1, and CR3 slightly propagate to the outer side (i.e., westward and eastward) with time, although XR1 and XR3 clearly grow southward and northward, as noted in Section 4.1. Therefore, it is suggested that the C5.1, C9.7, and X1.0 flares occur serially, corresponding to almost the same magnetic structures. In other words, the X1.0 flare is an extension of the C-class flares, and the X1.0 flare is driven by the reconnection of the magnetic field anchored in the outer region of the C-class flare ribbons.

4.3. Features of the Magnetic Fields

The vector magnetic field in the central part of the AR was observed by *Hinode*/SP between 11:00 and 11:33 UT, as shown in Figure 9. In panel (a), the white/black background indicates the positive/negative polarity of B_z. Green lines indicate the PILs (line of $B_z = 0$ G). The horizontal magnetic field vector $\boldsymbol{B}_h$ (red arrows) is overplotted on the B_z map. The horizontal field is strongly sheared along the PIL located between the P1 and N2 regions. It suggests that the major magnetic helicity along the PIL of the AR is negative. On the other hand, the vectors at the west side of the IPP stride over the PIL locally toward the northwest. It is consistent with the shape of the small bright loop connecting B1 and B2 in Figure 4(a). Therefore, the local magnetic field at the west side of the IPP has a positive magnetic helicity, which is opposite that of the major magnetic helicity along the PIL. It is more clearly seen in panel (b), which shows the relative shear angle χ, defined as the angle between the potential field $\boldsymbol{B}_p$ and the horizontal field $\boldsymbol{B}_h$ at each point. The black lines indicate the PILs, which is the same as the green lines in panel (a). The relative shear angle χ along the flaring PIL (between P1 and N2) and that on the west side of the IPP correspond to the shear angle θ_0 of the AR and the azimuth φ_e of the small magnetic disturbance in Kusano et al. (2012), respectively. Obviously, χ is around -90° (blue) along the PIL but χ is 90° (red) on the west side of the IPP. Therefore, the distribution of the relative shear angle χ suggests that the west side of the IPP satisfies the RS-type flare-trigger condition proposed by Kusano et al. (2012). They proposed that shear cancellation between the global magnetic field and the RS-type small magnetic field structure can trigger a flare, and significant brightenings should be observed in the solar atmosphere during the shear cancellation over the RS-type structure. In our case, significant

brightenings, B1 and B2, are observed at the west side of the IPP where the magnetic shear is opposite the shear of the global magnetic field along the flaring PIL. It is consistent with the theoretical prediction. Therefore, the west side of the IPP could be the location where the flares were triggered in the AR.

5. Discussion

5.1. Coronal Magnetic Field Extrapolation

In this study, we extrapolated the magnetic field in the corona, and compared it to the observed features. We derived the coronal magnetic field from the vector magnetic field data taken by HMI at October 25, 15:00 UT, using the NLFFF extrapolation method developed by Inoue et al. (2014). Figure 10 shows the coronal magnetic field lines anchored to the flare ribbons of the C9.7 and the X1.0 flares. The grayscale is an HMI LOS magnetogram at October 25, 15:00 UT. The red/blue contour outlines the brightenings (700 DN) in AIA 1600 Å, such as the flare ribbons observed at 15:50 UT/17:03 UT. The blue and orange tubes indicate the coronal magnetic field lines. The orange tubes are anchored to the ribbons of the C9.7 flare (CR1, CR2, and CR3), as shown in panels (a) and (b). On the other hand, the sky-blue tubes are anchored to the three ribbons of the X1.0 flare (XR1, XR2, and XR3), as seen in panels (c) and (d). The small magenta tubes indicated by the magenta arrow are the local magnetic field lines at the west side of the IPP. Obviously, the sky-blue magnetic loops connecting XR1 and XR3 are located at the outer edge of the orange loops connecting CR1 and CR3. These are consistent with the observed features that the flare ribbons of the X-class flare are on the outer side of the ribbons of the C-class flares, as shown in Figure 8.

5.2. Comparison with the Emerging Flux Model

Here, we discuss the flare-trigger scenario of consecutive C- and X-class flares by comparing with the theoretical model proposed by Chen & Shibata (2000). In this region, there are four kinds of possible magnetic connectivity: P1–N1, IPP–N1, IPP–N2, and P1–N2. Moreover, there is a filament trapped by the P1–N2 loops as seen in the AIA images (Figures 4, 6, and 7). If we focus on the connectivities IPP–N1 and P1–N2, the topology of the magnetic field is consistent with case B of Chen & Shibata (2000), in which the emerging flux appears on the outer edge of the filament channel. The IPP–N1 and P1–N2 connectivities have the same orientation relative to each other's main flaring PIL, and IPP–N1 can be considered as a flux emerging on the east edge of the filament channel P1–N2. Magnetic reconnection of the IPP–N1 flux, with the flux passing over the main flaring PIL (between P1 and N2), will weaken the latter flux. It can destabilize the current-carrying flux in the core region above the main flaring PIL, and the reconnection also produces short loops at the PIL between IPP–N2 and long loops connecting P1–N1.

In this scenario, to trigger an X-class flare, it is required that the flux rope exists on the PIL and that the flux rope erupts. The former is likely because a multitude of flares including three X-class flares had occurred in the same PIL between P1–N2. However, the latter is not consistent with the observed features that the filament along the PIL between P1–N2 does not move through the two C-class and X-class flare processes (cf. Figure 4). It indicates that the eruption of the flux rope, such as that required in the case B scenario, is unlikely. Moreover, the IPP is intruding onto N1, i.e., the magnetic loop connecting IPP–N1 moves away from P1–N2, as the IPP emerges; this is described in Section 4.1. This motion is in contrast to the scenario expected in case B of Chen & Shibata (2000), which requires that IPP–N1 approach P1–N2. Therefore, the flare trigger by the case B scenario may be difficult, although the magnetic field topology is consistent with this case.

5.3. Comparison with the RS-type Model

Another flare-trigger scenario is the RS type, which is proposed by Kusano et al. (2012). In this scenario, the key structure is the small magenta loops connecting IPP–N2, which are indicated by the magenta arrow in Figure 10. We found that the west side of the IPP satisfied the condition of the RS-type flare-trigger field based on the distribution of the relative shear angle (cf. Figure 9(b)). The long orange loops connecting P1–N1 are topologically equivalent to the overlying blue field line in Figures 4(a)–(c) of Kusano et al. (2012). Therefore, the following scenario is conceivable.

(1) Step-1 (trigger for the C-class flares). Magnetic shear cancellation proceeds between the IPP–N2 (magenta) loops and the P1–N1 (orange) loops at the west side of the IPP. The shear-canceling reconnection locally heats the atmosphere and causes chromospheric evaporation above the west side of the IPP. These local heating and evaporation are observed as the brightenings B1, B2, and B3 in the AIA images (Figures 2–4). The reconnected fluxes are transferred into the small loops connecting IPP–N1 and P1–N2, and the magnetic pressure above the west side of the IPP must decrease. The loops IPP–N1, P1–N1, and P1–N2 are heated by the reconnection. These are observed as the bright coronal loops L1, L2, and L3 in AIA 131 Å (Figure 5), although the location of the negative footpoint of L3 is fuzzy. The schematics of the magnetic field line before and after step-1 reconnection are shown in Figures 11(a) and (b). The orange and magenta loops are equivalent to the P1–N1 (orange loops) and IPP–N2 (magenta loops) loops in Figures 10(a) and (b). The small green loops in Figure 11(b) represent the small loops formed by the magnetic reconnection between the RS-type trigger field (magenta loops) and the overlying sheared field (orange loops).

(2) Step-2 (reconnection of the C-class flares). The sheared loop P1–N1 collapses inward because an inflow (such as that studied by Ugai & Shimizu 1996) drags flux into the region where magnetic pressure was decreased by the step-1 reconnection, i.e., above the west side of the IPP. Then, reconnection occurs in the collapsed loops (inside the orange loops connecting P1–N1 in Figures 10, 11(b)), and it shows the three ribbons CR1, CR2, and CR3 of the C5.1 and C9.7 flares. The reconnection is observed as the tether-cutting reconnection in the AIA 171 Å (Figure 6 and Movie 1) and 193 Å (Figure 7) images. Note that the CR2 in the IPP was the brightening B3 in the pre-flare phase, and that the brightening in the IPP represents the intensive electric current layer formed by the step-1 reconnection (see the Appendix).

(3) Step-3 (trigger for the X1.0 flare). It is inferred that the long twisted flux rope connecting P1–N1 might be formed by the tether-cutting reconnection, as illustrated by the thick orange line in Figure 11(c), according to Moore et al. (2001) and Kusano et al. (2012). There are other sheared loops (sky-blue loops connecting P1–N1 and P1–N2) above the orange loops and the long twisted flux rope. The flux rope gradually rises upwards with the overlying sky-blue loops, then the

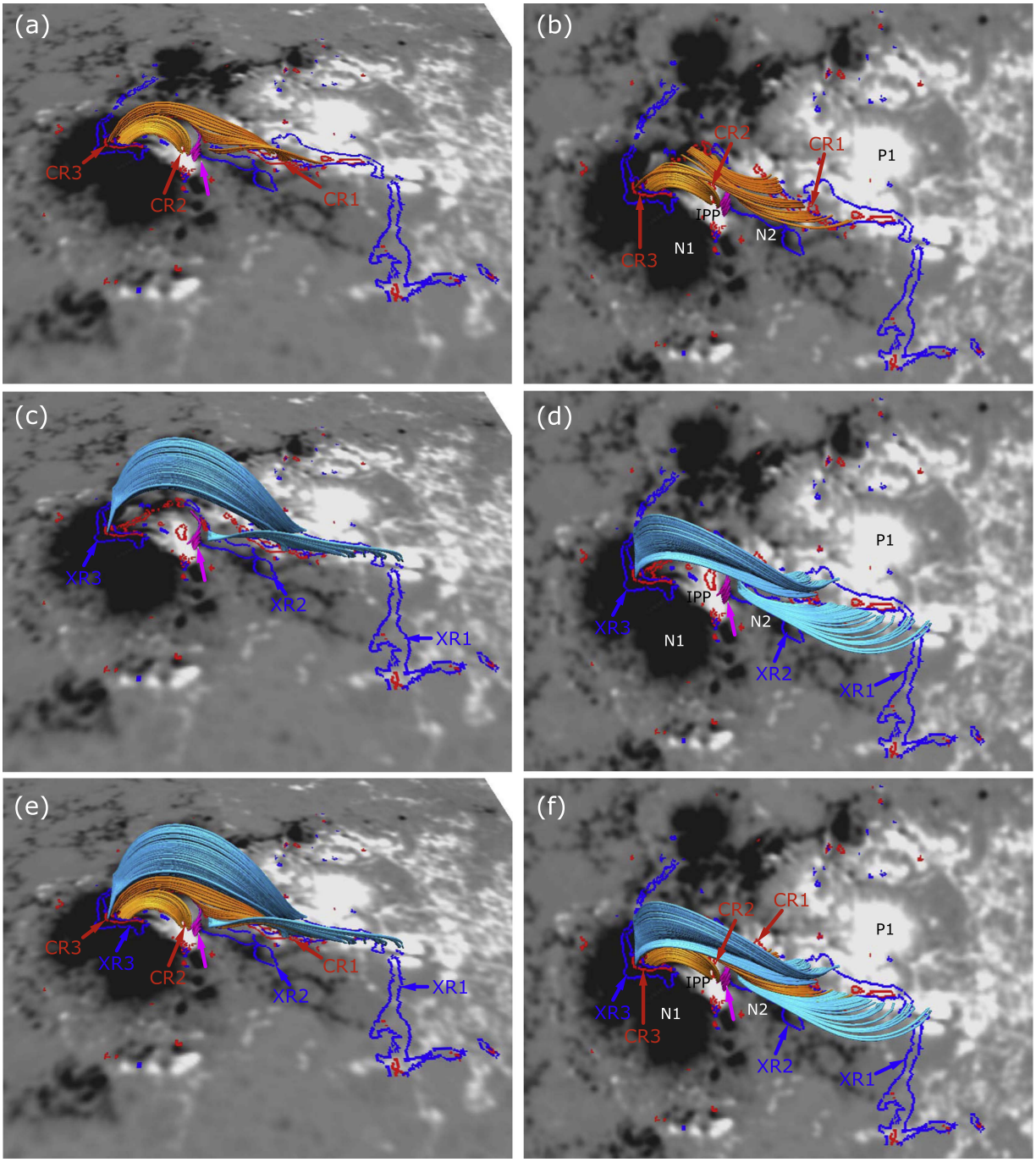

Figure 10. Magnetic field lines extrapolated using the NLFFF method. The left/right columns show a bird's eye view/top view of the same image. The grayscale images are the HMI LOS magnetograms taken on October 25, 15:00 UT. The red/blue contour outlines the brightenings (700 DN) in AIA 1600 Å such as the flare ribbons on 15:50 UT/17:03 UT. The small magenta tubes indicated by the magenta arrows are the local magnetic field lines at the west side of the IPP. The orange/sky-blue tubes indicate the coronal magnetic field lines anchored to the flare ribbons of the C9.7/X1.0 flare in panels (a) and (b)/(c) and (d), respectively. All the coronal magnetic field lines are plotted in panels (e) and (f).

magnetic fluxes are transferred upward, and the magnetic pressure over the PIL between the P1 and N1 regions decreases. After the magnetic pressure is decreased sufficiently, magnetic reconnection between the sky-blue loops occurs. It causes the X1.0 flare and produces the three ribbons (XR1, XR2, and XR3) at the footpoints of the sky-blue loops. The reconnection might produce a further long twisted flux rope connecting P1–N1, then the flare ribbons XR1 and XR3 are elongated to the south and north as magnetic reconnection with different field lines.

Therefore, the C5.1 and C9.7 flares can be originally triggered by the RS-type structure (the magenta loops connecting the IPP–N2) at the west side of the IPP, and the rise of the flux rope formed by the C-class flares triggers the X1.0 flare, in a three-step process. In Kusano et al. (2012), they put a small bipole that satisfies the RS-type condition just above the highly sheared PIL. Then, shear cancellation (step-1 reconnection) between the trigger field and the pre-existing sheared field occurs on the PIL. However, in the current AR, the IPP–N2 magenta loops are not located on the PIL between the major

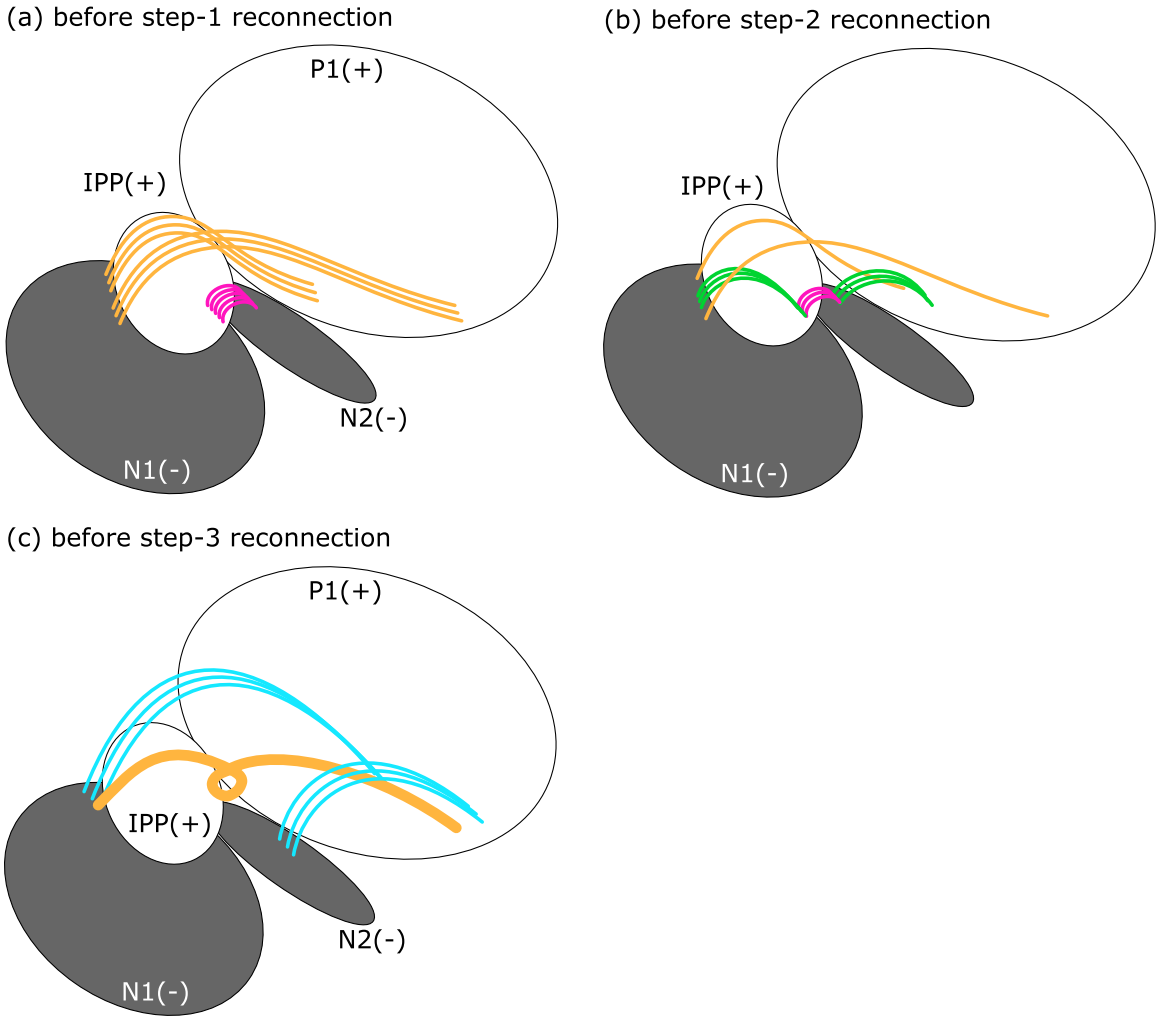

Figure 11. Schematics of the magnetic field lines before step-1, step-2, and step-3 reconnection. White/gray indicates the positive/negative polarity of the LOS magnetic field. (a) Before step-1 reconnection. The orange and magenta loops illustrate the P1–N1 and IPP–N2 loops in Figures 10 (a) and (b). (b) Before step-2 reconnection (i.e., after step-1 reconnection). The orange and magenta loops are the same as those in panel (a). The green loops indicate the small loops connecting IPP–N1 and P1–N2, which are formed by the flux cancellation between the orange and magenta loops. (c) Before step-3 reconnection. The sky-blue loops are equivalent to the P1–N2 and P1–N1 loops in Figures 10(c) and (d). The thick orange line illustrates the flux rope that is formed by step-2 reconnection under the sky-blue loops.

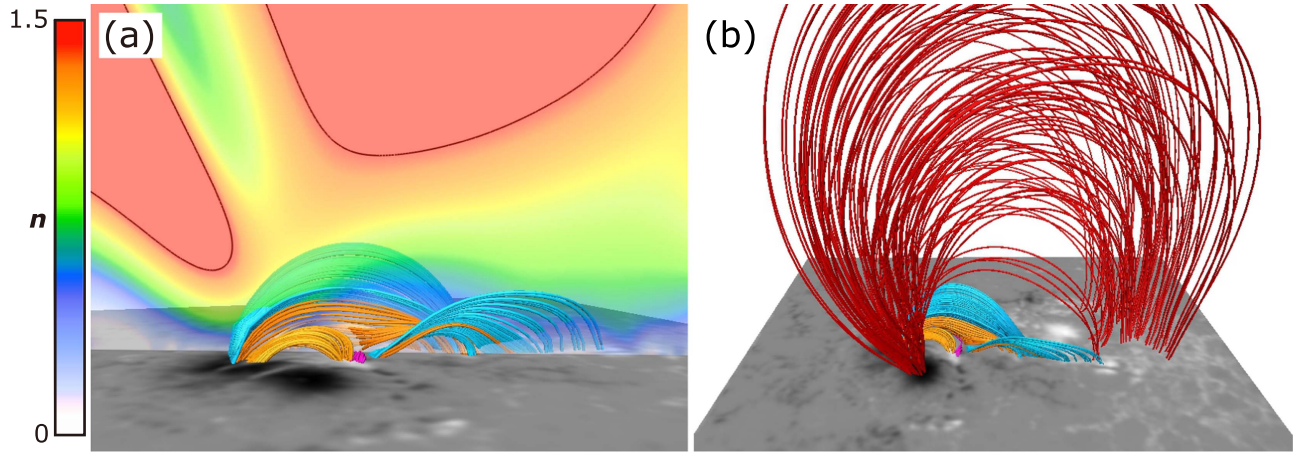

Figure 12. Coronal magnetic field lines from a side view of Figure 10(f). The vertical cross-section in panel (a) displays the decay index n between 0 and 1.5. The decay index n is calculated form the horizontal component of the potential field extrapolated from the vector magnetic field. The black line on the vertical cross-section indicates $n = 1.5$, which corresponds to the critical value for the torus instability. The red loops in panel (b) are closed loops over the highly sheared loops (the orange and the sky-blue loops). Obviously, the highly sheared loops corresponding to the C9.7 and the X1.0 flares are lower than the isosurface of $n = 1.5$, and there are closed loops over the sheared loops.

flare ribbons XR1 and XR2, i.e., the flare-trigger field is located slightly off the main flaring PIL. In the Appendix, we discuss the applicability of the RS-type scenario in the case of a trigger field that exists far from the main flaring PIL. According to an extra simulation, an RS-type field can work as a trigger of the flare even if it is located away from the highly sheared PIL. It is suggested that the RS-type flare-trigger process has a certain flexibility with the distance of the flare-trigger field from the highly sheared PIL.

5.4. Interpretation of "No CME Occurrence"

Figure 12(a) is the side view of Figure 10(f) in which the vertical cross-section displays the decay index n between 0 and 1.5. The decay index is defined as $n = -d\ln|\boldsymbol{B}_{p,h}|/d\ln|z|$, where $\boldsymbol{B}_{p,h}$ and z are the horizontal component of the potential magnetic field calculated from the observed B_z and the height, respectively (e.g., Shafranov 1966; Kliem & Török 2006). Obviously, the coronal magnetic loops anchored to both the C9.7 and the X1.0 flare ribbons have not reached the isosurface of $n = 1.5$, and the flux tube remained stable because the overlying magnetic field above the flux tube did not reach the critical decay index. Therefore, the highly sheared magnetic loops, which are related to the flares, have not satisfied a condition of the torus instability, although they satisfy the flare-trigger condition summarized in Inoue et al. (2015). In other words, the closed loops (red loops in panel (b)), which are over the orange and the sky-blue loops, might prohibit the twisted flux rope, which is created in the central part of the AR via tether-cutting reconnection with the C- and X-class flares, from erupting (Inoue et al. 2016).

According to Kusano et al. (2012), the causality between the flux rope eruption, which may create CMEs, and the magnetic reconnection of flares is different between the two types of flare-trigger processes. The RS-type flare-trigger process is a "reconnection-induced eruption" process where the tether-cutting reconnection of the flare is triggered before the eruption of the flux rope. It means that the RS-type flare does not necessarily cause a large flux rope eruption such as a CME. Therefore, it is also consistent that the flares triggered by the RS-type magnetic configuration did not have an associated CME in the AR.

6. Summary

In this study, we analyzed the X1.0 flare and the two preceding C-class flares that occurred in AR NOAA 12192. We aimed to clarify the triggering process and to evaluate the applicability of a flare-trigger model such as that proposed by Kusano et al. (2012). We analyzed the filter and vector magnetograms from *Hinode*/SOT and *SDO*/HMI, and also used the filtergrams for each layer of the solar atmosphere from *SDO*/AIA. We found that there was a characteristic magnetic field structure, which is the positive polarity intruding on the following negative sunspot (we named the structure "the IPP"). Significant chromospheric brightenings and coronal loops were also observed around the IPP before the onset of the flares. The relative shear angle χ, which is defined as the angle between the potential field vector and the horizontal field vectors, was measured in the AR. These observed features were consistent with the RS-type flare-trigger field of the KB12 model. We considered the flare-trigger scenario from the coronal magnetic loops that were extrapolated using the NLFFF method. The triggering process of the flares was more consistent with the RS type of the KB12 model rather than case B of Chen & Shibata (2000), because the former does not require an epic eruption of the flux rope to trigger the flare. Therefore, we concluded that the RS type of the KB12 model is more suitable for the triggering process of C-class flares, and that the X1.0 flare was caused by the rise of the flux rope formed by the preceding C-class flares, in a three-step process.

In the AR, the RS-type field was located slightly off the main flaring PIL whereas the RS-type field is injected just above the highly sheared PIL in the original RS-type simulation. According to an extra simulation with the RS-type field offset from the highly sheared PIL (see the Appendix), it is suggested that the RS-type flare-trigger process has a certain flexibility for the distance of the flare-trigger field from the highly sheared PIL. However, it is still unclear how a distant field that is away from the PIL can trigger flares on the actual solar surface. We need to statistically investigate the distance between the flaring PILs and the flare-trigger fields using observational data.

We also discussed the causality between these flares and CMEs by considering the critical height of the onset of the torus instability. The closed magnetic field overlying a flux rope, which might be created by tether-cutting reconnection between the highly sheared loops, has not reached the critical decay index, and it might prohibit the flux rope from erupting. In addition, this was also consistent with our conclusion that the C5.1, C9.7, and X1.0 flares were triggered by the RS-type field, which might cause reconnection without the help of eruptive instabilities such as the torus instability. This suggests that the magnetic reconnection might not have developed substantially, and that the flux rope did not reach a condition of the torus instability.

In AR 12192, five more X-class flares occurred with the growth of the positive polarity that is intruding on the following negative polarity region. These X-class flares showed clear two-ribbon structures at similar locations, and there were no CMEs associated with the X-class flares. We suggest that the west side of the IPP could be a trigger of these X-class flares although we need a detailed analysis for each flare event. Sun et al. (2015) reported that the electric current along the flaring PIL was very low, and the horizontal magnetic field decreased much slower with height, before the X3.1 flare on October 24 ($\sim$20 hr before the X1.0 flare). Thalmann et al. (2015), using global magnetic field modeling, also pointed out that the strong closed arcade over the highly sheared arcades contributed to the confinement of the flux rope for several M-class and X-class flares that occurred in AR 12192. Therefore, a similar magnetic configuration might remain during the AR disk passage, and it is important to investigate the temporal evolution of the characteristic magnetic structures in order to clarify the conditions of these "consecutive" and "confined" flares. The combination of *Hinode* and *SDO* observations and NLFFF extrapolations is a powerful tool for analyzing local and global magnetic field changes in the AR.

We are grateful to Dr. David H. Brooks and *Hinode* group members in ISAS/JAXA for useful discussions. The HMI and AIA data were used courtesy of NASA/*SDO* and the AIA and HMI science teams. *Hinode* is a Japanese mission developed and launched by ISAS/JAXA, which collaborates with NAOJ as a domestic partner and with NASA and STFC (UK) as

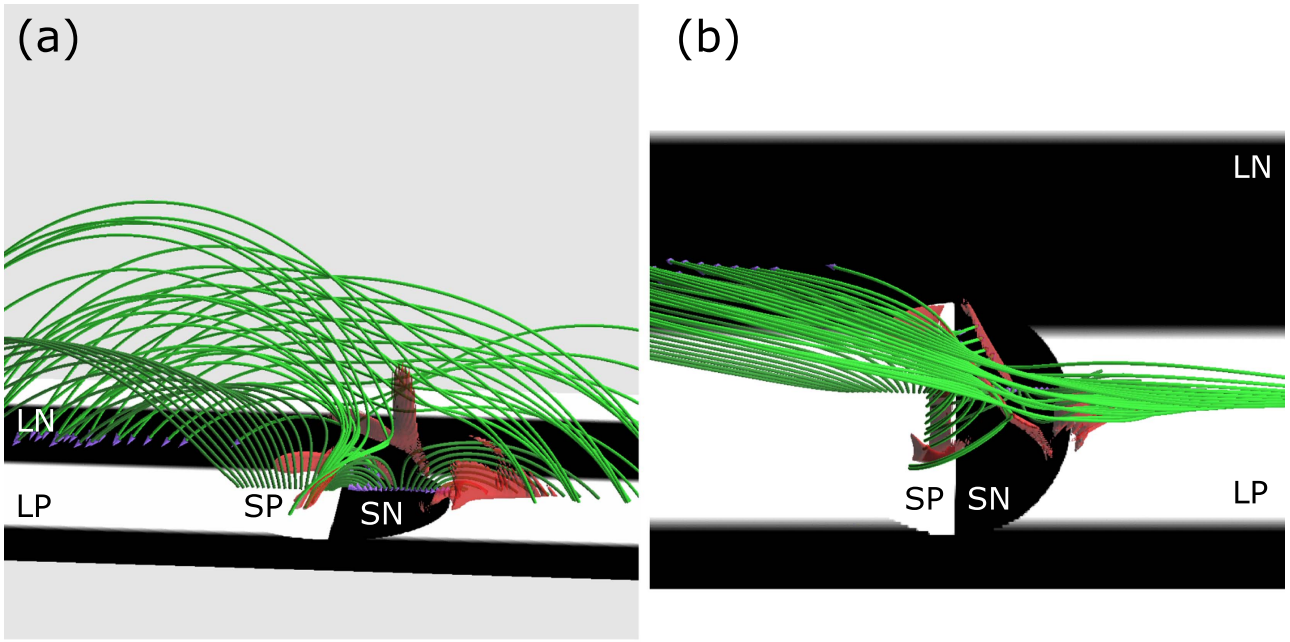

Figure 13. Snapshot of the KB12 model simulation with an offset of the RS-type field from the PIL. White and black areas indicate the positive and negative magnetic polarity areas, respectively. Green tubes represent the magnetic field lines, and red surfaces correspond to the intensive current layers. Both (a) and (b) show the same snapshot, but the bird's eye view and top view are shown in panel (a) and (b), respectively.

international partners. Scientific operation of the *Hinode* mission is conducted by the *Hinode* science team organized at ISAS/JAXA. This team mainly consists of scientists from institutes in the partner countries. Support for the post-launch operation is provided by JAXA and NAOJ (Japan), STFC (UK), NASA, ESA, and NSC (Norway). This work was partly carried out at the NAOJ *Hinode* Science Center, which is supported by MEXT KAKENHI Grant Number 17GS0208, by generous donations from Sun Microsystems, and by NAOJ internal funding. The *Hinode* Science Center at Nagoya University also supported the study. Part of this work was carried out on the Solar Data Analysis System operated by the Astronomy Data Center in cooperation with the *Hinode* Science Center of the NAOJ. We plotted the magnetic field lines extrapolated by NLFFF method using VAPOR, which is a product of the National Center for Atmospheric Research's Computational and Information Systems Lab. This work was supported by JSPS KAKENHI Grant Numbers 16H07478, 23340045, 15H05814, and Grant-in-Aid for JSPS Fellows. We thank anonymous referees for carefully reading our manuscript and for making useful comments.

Appendix

Figure 13 shows a snapshot of an extra simulation in which the RS-type bipole field is injected off the PIL. The white/black area indicates the positive/negative magnetic polarity area, and the green tubes represent the magnetic field lines. The red surfaces correspond to the intensive electric current layers. The major bipole is comprised of the large positive (LP) and the large negative (LN) regions, and the major PIL is located between the LP and LN. The small-scale bipole field, which satisfies the RS-type condition, intrudes into the LP region, and it is comprised of the small positive (SP) and the small negative (SN) regions. Note that the RS-type bipole field intrudes on the positive polarity region while the IPP (positive polarity) intrudes on the negative polarity (N1) region in AR 12192. Moreover, the magnetic helicity in the simulation is positive while the magnetic helicity in the analyzed AR is negative.

Figure 13 shows the snapshot between step-1 and step-2 reconnection, i.e., between the internal reconnection and flare reconnection of the RS scenario in the KB12 model. The overlying field connecting LP–LN and the small bipole field SP–SN is equivalent to the P1–N1 loops (orange loops) and the IPP–N2 loops (magenta loops) in Figures 10 and 11, respectively. The small loops connecting SP–LN and LP–SN are equivalent to IPP–N1 and P1–N2 (green loops in Figure 11(b)). The vertical electric current layer is formed over the center of the SN region as the step-1 reconnection proceeds between the LP–LN and SP–SN loops. This vertical electric current is observed as the brightening B3 and CR2 in the AIA 1600 and 304 Å images (Figures 2 and 4). Then the large-scale sheared loops (LP–LN) collapse inward and the flare ribbons appeared at the footpoints in the LP and LN regions. These ribbons are equivalent to CR1 and CR3 of the C-class flares. Therefore, the locations of the intensive electric current layer are consistent with the RS-type case.

Moreover, the twisted flux rope, which is formed by the reconnection between the LP–LN and SP–SN loops, asymmetrically rise up from the LN side in the simulation. In the analyzed AR, the flux rope illustrated by the thick orange line in Figure 11 starts erupting from the P1 side. Therefore, the step-3 reconnection of the sky-blue loops connecting P1–N2 occurs earlier with the asymmetric rise of the underlying flux rope, and the flare ribbons XR1 and XR2 appear earlier than XR3.

References

Antiochos, S. K., DeVore, C. R., & Klimchuk, J. A. 1999, ApJ, 510, 485
Bamba, Y., Kusano, K., Imada, S., & Iida, Y. 2014, PASJ, 66, S16

Bamba, Y., Kusano, K., Yamamoto, T. T., & Okamoto, T. J. 2013, ApJ, 778, 48
Carmichael, H. 1964, NASSP, 50, 451
Chen, P. F., & Shibata, K. 2000, ApJ, 545, 524
Gary, G. A., & Hagyard, M. J. 1990, SoPh, 126, 21
Green, L. M., Kliem, B., & Wallace, A. J. 2011, A&A, 526, A2
Hagyard, M. J., Teuber, D., West, E. A., & Smith, J. B. 1984, SoPh, 91, 115
Heyvaerts, J., Priest, E. R., & Rust, D. M. 1977, ApJ, 216, 123
Hirayama, T. 1974, SoPh, 34, 323
Inoue, S., Hayashi, K., & Kusano, K. 2016, ApJ, 818, 168
Inoue, S., Hayashi, K., Magara, T., Choe, G. S., & Park, Y. D. 2015, ApJ, 803, 73
Inoue, S., Magara, T., Pandey, V. S., et al. 2014, ApJ, 780, 101
Kliem, B., & Török, T. 2006, PhRvL, 96, 255002
Kopp, R. A., & Pneuman, G. W. 1976, SoPh, 50, 85
Kosugi, T., Matsuzaki, K., Sakao, T., et al. 2007, SoPh, 243, 3
Kurokawa, H., Wang, T., & Ishii, T. T. 2002, ApJ, 572, 598
Kusano, K., Bamba, Y., Yamamoto, T. T., et al. 2012, ApJ, 760, 31
Kusano, K., Maeshiro, T., Yokoyama, T., & Sakurai, T. 2004, ApJ, 610, 537
Kusano, K., Suzuki, Y., & Nishikawa, K. 1995, ApJ, 441, 942
Lemen, J. R., Title, A. M., Akin, D. J., et al. 2012, SoPh, 275, 17
Lin, R. P., Dennis, B. R., Hurford, G. J., et al. 2002, SoPh, 210, 3
Lites, B. W., & Ichimoto, K. 2013, SoPh, 283, 601
Lites, B. W., Low, B. C., Martinez Pillet, V., et al. 1995, ApJ, 446, 877
Louis, R. E., Puschmann, K. G., Kliem, B., Balthasar, H., & Denker, C. 2014, A&A, 562, A110
Moore, R. L., Sterling, A. C., Hudson, H. S., & Lemen, J. R. 2001, ApJ, 552, 833
Ogawara, Y., Acton, L. W., Bentley, R. D., et al. 1992, PASJ, 44, L41
Pesnell, W. D., Thompson, B. J., & Chamberlin, P. C. 2012, SoPh, 275, 3
Schou, J., Scherrer, P. H., Bush, R. I., et al. 2012, SoPh, 275, 229
Shafranov, V. D. 1966, RvPP, 2, 103
Sturrock, P. A. 1966, Natur, 211, 695
Sun, X., Bobra, M. G., Hoeksema, J. T., et al. 2015, ApJL, 804, L28
Thalmann, J. K., Su, Y., Temmer, M., & Veronig, A. M. 2015, ApJL, 801, L23
Tsuneta, S. 1996, ApJ, 456, 840
Tsuneta, S., Hara, H., Shimizu, T., et al. 1992, PASJ, 44, L63
Tsuneta, S., Ichimoto, K., Katsukawa, Y., et al. 2008, SoPh, 249, 167
Ugai, M., & Shimizu, T. 1996, PhPl, 3, 853
Yashiro, S., Akiyama, S., Gopalswamy, N., & Howard, R. A. 2006, ApJL, 650, L143
Zhang, H. 2001, ApJL, 557, L71